Multi-point observations of modulated whistler-mode waves and energetic electron precipitation

Murong Qin[1,2], Wen Li[1], Qianli Ma[1,4], Leslie Woodger[3], Robyn Millan[3], Xiao-Chen Shen[1], and Luisa Capannolo[1]

[1] Center for Space Physics, Boston University, Boston, Massachusetts, USA.

[2] Cooperative Programs for the Advancement of Earth System Science, UCAR, Boulder, Colorado, USA.

[3] Department of Physics and Astronomy, Dartmouth College, Hanover, New Hampshire, USA.

[4] Department of Atmospheric and Oceanic Sciences, University of California, Los Angeles, California, USA.

Corresponding author: Murong Qin (mqin1@bu.edu); Wen Li (wenli77@bu.edu)

Key Points:

- Modulated energetic electron precipitation is observed by BARREL at $L \sim 6$ from noon to dusk.
- Whistler-mode waves observed by RBSP-B are well correlated with electron precipitation both in the plumes and plasma trough.
- Modulation of the modeled electron precipitation driven by whistler-mode waves is consistent with the enhancement in BARREL X-rays.

Abstract

In this study, we present simultaneous multi-point observations of whistler-mode waves detected by RBSP-B, associated with conjugate electron precipitation observed through enhanced BARREL X-rays at $L \sim 6$ from noon to dusk. Both long period modulation at periods of several to tens of minutes and short period modulation at about tens of seconds are observed in X-ray measurements. Similar periodicities are also observed for whistler-mode wave amplitude. We show that the correlation coefficient between whistler-mode waves and electron precipitation is high in several regions, including plumes and plasma trough. Ultra-Low-Frequency (ULF) waves (8–30 mHz), which have been suggested to play a potential role in precipitating electrons by modulating whistler-mode wave intensity or loss cone size, show a weak correlation with whistler-mode wave amplitudes and the X-ray counts during the conjunction. We further evaluate whistler-mode wave driven electron precipitation using a physics-based technique. The time evolution of the modeled electron precipitation is found to be remarkably consistent with the modulation in the BARREL X-ray counts both in plumes and plasma trough. By taking advantage of the high-resolution wave data and close conjunction, we provide strong evidence that whistler-mode waves are not only directly responsible for the longer modulation (several to tens of minutes), but also the shorter modulation (tens of seconds) of the electron precipitation.

Plain Language Summary

Whistler-mode waves, which are right-handed polarized electromagnetic plasma waves commonly observed in the Earth's inner magnetosphere, have been known to be efficient in precipitating electrons. Extensive studies have revealed the pitch angle scattering of energetic electrons caused by whistler-mode waves in the plasmasphere (near-Earth regions where cold and dense plasmas are corotating with the Earth) or in the plasma trough (regions further away from the Earth where cold plasmas are less dense). However, the role of whistler-mode waves in the plasmaspheric plumes (the extension of the plasmasphere at further distances from the Earth), especially the temporal and spatial evolution of plume whistler-mode waves and associated energetic electron precipitation, requires further investigation. In the present study, by taking advantage of multi-point measurements, we evaluate the time evolution of whistler-mode wave driven energetic electron precipitation in both the plumes and the plasma trough regions, with waves observed by RBSP-B near the equator and electron precipitation detected through enhanced X-rays observed by BARREL. We show that whistler-mode waves in both the plumes and the plasma trough account for the energetic electron precipitation, which is essential to understand the radiation belt electron dynamics.

1 Introduction

Whistler-mode chorus and hiss waves have been suggested to be effective in driving energetic electron precipitation into the atmospheric loss cone. Whistler-mode chorus waves are commonly observed in two distinctive bands, i.e., lower band with a frequency range of 0.1–0.5 f_{ce} and upper band with a frequency range of 0.5–0.8 f_{ce}, where f_{ce} is the equatorial electron gyrofrequency. Chorus waves can effectively precipitate electrons and have been known to be the main driver of diffuse (Ni et al., 2008, 2011) and pulsating aurorae (Nishimura et al., 2010). Plasmaspheric hiss (tens of Hz to a few kHz) is an incoherent, broadband whistler-mode emission. Hiss waves have been suggested to be responsible for the slow decay of radiation belt electrons, leading to the

formation of the quiet-time slot region (Lyons et al., 1972; Lyons & Thorne, 1973). Hiss waves have not only been extensively detected in the plasmasphere (Thorne et al.,1973; Meredith et al., 2004), but also in the plasmaspheric plumes (Chan & Holzer, 1976; Shi et al., 2019; Su et al., 2018), detached or attached regions of the plasmasphere drained sunward toward the dayside magnetopause in the afternoon sector during enhanced plasma convection (Carpenter et al., 2000; Chen & Wolf, 1972; Goldstein et al., 2004; Moldwin et al., 2004).

There is growing interest in plume whistler-mode wave driven energetic electron precipitation. Borovsky & Steinberg (2006) found that dropout of the radiation belt electrons often coincided with plasmaspheric plumes at geosynchronous orbit, suggesting that plume hiss potentially plays a role in precipitating energetic electrons. Summers et al. (2008) investigated electron precipitation driven by plume hiss observed by the CRRES satellite. It was shown that plume hiss can effectively precipitate ~100 keV energetic electrons into the loss cone and affect the generation of MeV electrons by reducing the seed population. Plume hiss waves are further shown to effectively scatter electrons into the loss cone (~10 to 100 keV) within a few days, leading to their rapid loss (Zhang et al., 2018, 2019). Despite previous studies that have suggested the potential importance of plume hiss waves, simultaneous observations of plume hiss waves and energetic electron precipitation are rare. Li et al. (2019) reported plume whistler-mode wave driven energetic electron precipitation by analyzing conjunction events observed by Van Allen Probes and POES. Though the observation of electron precipitation caused by hiss waves has been shown to be consistent with quasi-linear theory, the quantification of the temporal and spatial dynamics of precipitation is still needed.

The BARREL campaigns, which were conducted during the Van Allen Probes mission (also known as RBSP; Mauk et al., 2013), provide measurements of bremsstrahlung X-rays generated by precipitating electrons as they interact with the atmosphere (Millan et al., 2013; Woodger et al., 2015). Since the BARREL platform drifts slowly in space, evaluation of the temporal evolution of electron precipitation is allowed. Breneman et al. (2020) presented modulated X-ray enhancements driven by plume hiss in association with solar wind dynamic pressure variations (tens of minutes); however, the quantitative calculation of hiss-driven electron precipitation was difficult because of the lack of high-frequency-resolution wave data from THEMIS during this event. The modulation of X-rays on several minutes has been shown in Breneman et al. (2015) and was suggested to be directly driven by plasmaspheric hiss.

In the present paper, we report and quantitatively analyze the modulation of X-rays generated by energetic electron precipitation both on a long-time scale (several to tens of minutes) and a short time scale (< 2 min) and its correlation with the whistler-mode waves in plumes and the plasma trough, detected by RBSP-B. Concurrent X-ray enhancements detected by BARREL provided evidence of electron precipitation associated with the whistler-mode waves. The close conjunction between RBSP and BARREL provides a unique opportunity to perform an in-depth analysis of the whistler-mode wave modulated electron precipitation. The content of the paper is outlined below. An overview of the event and detailed whistler-mode wave properties are presented in section 2. In section 3, we discuss the correlation between the measured whistler-mode emissions and BARREL X-rays, and through a physics-based method using the quasi-linear theory, the modulation of the modeled electron precipitation with the observed modulated X-rays is compared. Results and conclusions are discussed and summarized in section 4.

2 Observations

2.1 Event overview

Figure 1 shows an overview of the conjunction event, with waves observed by RBSP-B and enhanced X-rays observed by BARREL 3E. Figures 1a–1b show the calculated L and MLT for RBSP-B (blue) and BARREL-3E (red) based on the T89 magnetic field model (Tsyganenko, 1989). The separation between RBSP-B and BARREL was within $\Delta L = 1$ and $\Delta\mathrm{MLT} = 1$ h over 10:40–14:32 UT, as marked by the black vertical dashed lines. Both RBSP-B and BARREL drifted slowly from noon to dusk during this time period. The close conjunction and slow drift of BARREL and RBSP-B indicate that the variations were mostly temporal. During the conjunction, RBSP-B detected moderate whistler-mode wave emissions, which are shown in Figure 1c. The superimposed magenta line represents electron number density inferred from the upper hybrid resonance frequency identified from the EMFISIS High Frequency Receiver (HFR) (Kletzing et al., 2013) spectral data onboard RBSP-B (Kurth et al., 2015). Whistler-mode wave emissions were detected both in high-density plumes and low-density plasma trough.

EMIC waves, which are known to effectively scatter relativistic electrons (Z. Li et al., 2013; Qin et al., 2018, 2019, 2020; Summers et al., 2003;) as well as ~100s keV electrons (Capannolo et al., 2019a, 2019b; Chen et al., 2016; Clilverd et al., 2015; Hendry et al., 2017), were not detected within the conjunction region (Figure 1d), and thus were unlikely to play a role in this precipitation event. It is also suggested that ULF waves could play a potential role in precipitating energetic electrons, either by modulating the whistler-mode wave intensity (Breneman et al., 2015, 2020; Halford et al., 2015； Jaynes et al., 2015) or transporting particles radially inward where the loss cone becomes larger (Brito et al., 2012, 2015). During conjunction with BARREL-3E in our case, RBSP-B detected moderate ULF waves which were analyzed based on the EMFISIS (Kletzing et al., 2013) magnetometer measurement with 4-s resolution, as shown in Figure 1e. The horizontal lines in panel (e) indicate frequencies of 8 mHz and 30 mHz, and ULF waves within this frequency range were selected to show modulations below the 2-min period. The observed waves in the conjunction region were associated with the enhancement of the 25–48 keV and 48–95 keV BARREL X-rays, as shown in the fast spectrum (Millan et al., 2013; Woodger et al., 2015) in Figure 1f. The balloon detected X-rays are mainly generated by the interaction between the atmospheric constituents and <100 keV precipitating electrons (Jaynes & Usanova, 2019). We further evaluate whether whistler-mode hiss waves (Period I) and chorus waves (Period II) are fully responsible for the electron precipitation, whether ULF waves are modulating the whistler-mode waves, or whether ULF waves are the direct cause of the precipitation, as discussed in Section 2.2. Although highly-correlated intense chorus waves and X-rays were observed during 11:45–12:15 UT, this period was not further analyzed due to the data gaps in the BARREL observation.

The whistler-mode wave properties during the conjunction are further analyzed in Figure 2. Figure 2a shows total electron density inferred from the upper hybrid resonance frequency (magenta line) and spacecraft potential (black line). The whistler-mode waves observed over 11:10–11:25 UT (Period I) were located in the plume region, as indicated by the elevated electron density compared to the plasma trough region after 11:25 UT, where chorus waves were observed. Figures 2b–2d show the magnetic spectral density, ellipticity and wave normal angle of the waves. The waves with the frequency from 100 Hz to a few kHz are right-hand polarized with small wave normal angles. Magnetic waveform data from the EMFISIS search coil magnetometer shows that these

155 emissions are hiss-like whistler-mode waves rather than discrete chorus waves inside the plume
156 region (not shown). The MagEIS (Blake et al., 2013) instrument onboard RBSP-B observed an
157 enhancement of electron flux peaking at 90^o pitch angle in the 54 keV energy channel, as shown
158 in Figure 2e. The increased temperature anisotropy might contribute to the observed whistler-
159 mode wave growth. Although magnetosonic waves were also observed during the period, they
160 typically accelerate the electrons at higher pitch angles only and are unlikely to directly cause the
161 observed energetic electron precipitation (Ma et al., 2016).
162

166 **2.2 Modulation of waves and electron precipitation**

167 In order to evaluate whether the observed electron precipitation is correlated with the whistler-
168 mode waves or ULF waves, we show the correlation coefficients between them (Figure 3). The
169 amplitudes of the whistler-mode waves (black) observed by RBSP-B is shown in Figure 3a. The
170 whistler-mode wave amplitude is obtained by integrating the wave magnetic spectral intensity
171 measured by Waveform Receiver (WFR) from 200 to 2,000 Hz. Figure 3b shows the enhancement
172 of X-rays generated by electron precipitation observed by BARREL. Long period modulations on
173 a time scale of 5-60 minutes were observed in X-rays, which show clear similarities to the
174 modulation of whistler-mode wave amplitude. Such a slow modulation of wave amplitude and
175 electron precipitation has been suggested to be driven by modulation of the overall magnetosphere
176 cavity size (forced-breathing) (Breneman et al., 2020; Kepko & Spence, 2003; Kepko & Viall,
177 2019; Kepko et al., 2002). The magnetic field fluctuations obtained from the fluxgate
178 magnetometer waveform data were filtered to obtain the ULF wave amplitude between 8 and 30
179 mHz (33s to 2 min) in all three components, as shown in Figure 3c. To evaluate the correlation
180 between the observed waves and electron precipitation on a time scale shorter than 2 min, the ULF
181 wave amplitude and the X-ray count rates were interpolated to match the time resolution of
182 whistler-mode wave observations (6-s time resolution). Then the correlation coefficient was
183 calculated every 15 minutes with a time-shifted window of 2 minutes between X-ray count rate,
184 whistler-mode wave amplitude and ULF wave amplitude (8–30 mHz). The correlation coefficient
185 between whistler-mode wave amplitudes and X-ray count rates in the lowest energy channel 25–
186 48 keV is shown in Figure 3f, which is found to be especially high (~0.7) in the region of plumes
187 (Period I). The correlation coefficient between ULF and whistler-mode wave amplitudes is low
188 (Figure 3e) and the whistler-mode wave intensity in the region of plumes is likely modulated by
189 plasma density (Chen et al., 2012). The correlation coefficient between spacecraft potential which is
190 used to infer the plasma density and the whistler wave amplitude is ~0.8 (not shown here). In period
191 II, the highest correlation coefficient is ~0.7 between whistler-mode chorus waves and X-rays. It
192 is also worth noting that the correlation coefficient between 8–30 mHz ULF waves and X-rays
193 (Figure 3d) is much lower compared to that of whistler-mode waves and X-rays (Figure 3f) in
194 these two periods, suggesting that the role of 8–30 mHz ULF waves in the X-ray enhancement is
195 negligible.

196 **3 Comparison between observed and modeled electron precipitation**

197 We follow a physics-based technique to quantify the pitch angle scattering rates driven by the
198 moderately strong whistler-mode waves (Ma et al., 2020). The quasi-linear diffusion coefficients
199 based on whistler-mode wave frequency spectra and the background plasma parameters are
200 calculated with the Full Diffusion Code (Ni et al., 2008). Landau resonance and cyclotron
201 harmonic resonances (-10 to 10) are taken into account. It is assumed that whistler-mode wave

normal angles are quasi-parallel to the magnetic field line near the equatorial plane as supported by the RBSP-B observations (Figure 2d) and increase as magnetic latitudes increase (Ni et al., 2013). Plasma density is taken from the RBSP measurement and assumed to be constant along the field lines.

The long period structures (~10s of minutes) are shown in the bounce-averaged pitch angle diffusion coefficients at the loss cone ($<D_{\alpha\alpha}>_{LC}$) for electrons from 10 keV to 1 MeV in Figure 4b, which is calculated from the observed whistler-mode wave amplitude (Figure 4a), wave frequency spectrum, and the plasma density and magnetic field every 6 s. From Figure 4b, it can be seen that the observed whistler-mode waves can cause electron precipitation up to MeV and are most effective in precipitating electrons below 100 keV, with scattering rates up to 10^{-3} s^{-1} at the loss cone. This is consistent with the BARREL observation that only 25–95 keV X-rays, which are mainly generated by <100 keV electron precipitation (Jaynes & Usanova, 2019), are enhanced during this time period. The slow modulation in wave amplitude (Figure 4a) and $<D_{\alpha\alpha}>_{LC}$ (Figure 4b) best matches the count rate of 25–48 keV BARREL X-rays (the superimposed purple line) at periods of tens of minutes.

With the $<D_{\alpha\alpha}>_{LC}$ and the electron flux near the loss cone, we then determine the equatorial pitch angle distribution of electrons inside the loss cone using the solution for the Fokker-Planck equation under the quasi-equilibrium state (Kennel & Petschek, 1966; Li et al., 2013). The electron flux near the loss cone is calculated based on the electron flux measured by RBSP-B at the lowest pitch angle bin, as shown in Figure 4c. During the conjunction, the HOPE (Funsten et al., 2013) and MagEIS instruments on ECT (Spence et al., 2013) were only able to measure electrons with local pitch angles above 18^o and 24^o respectively, and the flux just outside the loss cone angle is approximately evaluated as the flux at the lowest pitch angle bin. Since the flux tends to fall off as pitch angle decreases, using the fluxes at 18^o–24^o pitch angles will likely lead to an upper limit estimate on the precipitation.

The equatorial electron pitch angle distributions are mapped to the 70 km using T89 magnetic field model. Figure 4d shows the energy spectrogram of electron fluxes averaged within the local loss cone, which indicates the precipitation of ~10s to ~100s of keV electrons especially when the whistler-mode wave amplitudes are modest or intense. The time evolution of the calculated electron precipitation is also roughly consistent with the enhancement in BARREL X-rays. The electrons with lower energies (~tens of keV) are subject to more efficient scattering loss than the higher-energy ones (above several hundred keV). The observed electron flux at the lowest pitch angle bin is roughly constant during the conjunction (Figure 4c), indicating that modulation in the modeled electron precipitation are caused by the modulation of the observed whistler-mode waves.

In addition to the large-scale modulation with periods of several to tens of minutes, fluctuations on a shorter time scale (< 2 min) have also been extensively observed in the BARREL data but are often neglected in previous studies. Breneman et al. (2015) investigated the global-scale modulation of whistler-mode wave driven electron precipitation. The modulation of X-rays generated by electron precipitation at periods > 1 min for an event studied on 3 January 2014 was found to be remarkably consistent with hiss wave amplitude; however, the fluctuation on a time scale of <1 min is not consistent between waves and electron precipitation. This might be caused by the large separation between the BARREL payload and the spacecraft and hiss wave intensity

might be modulated by the local plasma density. In our case, the separation between BARREL-3E and RBSP-B is small ($\Delta L < 1, \Delta MLT < 0.9$), allowing us to exclude the spatial effect. In order to evaluate the modulation between the observed waves and electron precipitation on a shorter time scale (<2 min), observations in Period I and Period II in Figure 4 are zoomed in to show more details. The results are shown in Figures 5 and 6 respectively. The wave amplitude of plume hiss waves shown in Figure 5a ranges from 5 pT to ~35 pT and the observed plume hiss waves are most effective in precipitating electrons around 30 keV, as shown in $<D_{\alpha\alpha}>_{LC}$ in Figure 5b. The wave amplitude of chorus waves shown in Figure 6a is about the same as the plume hiss waves. The chorus waves are more effective in precipitating electrons at lower energies (at least below ~30 keV) in our case, as shown in $<D_{\alpha\alpha}>_{LC}$ in Figure 6b. An almost one-to-one correlation was observed between the whistler-mode wave amplitudes and the enhancement in X-ray counts in both the plasmaspheric plumes and the plasma trough. The time evolution of the calculated $<D_{\alpha\alpha}>_{LC}$, which controls the pitch angle evolution and ultimate precipitation rate under the quasi-equilibrium state, was remarkably consistent with the modulation of X-rays measured by BARREL on the short time scale of less than 2 minutes. The correlation between the electron precipitation and the whistler-mode waves firmly demonstrates that the observed whistler-mode waves account for the energetic electron precipitation and can drive electron precipitation into the atmospheric loss cone.

4 Summary and Discussion

In this paper, we analyze a unique event when BARREL-3E was ideally situated to observe the enhancement of X-rays associated with the whistler-mode waves detected by RBSP-B. By analyzing the close conjunction event ($\Delta L < 1, \Delta MLT < 0.9$), we quantitatively investigate the role of whistler-mode waves in causing energetic electron precipitation, and their relation to the observed ULF waves. The main conclusions are the following.

(1) Energetic electron precipitation modulation was observed by BARREL at $L \sim 6$ from noon to dusk. Besides the previously proposed long period modulation on the time scale of 1–60 minutes (Breneman et al., 2015, 2020), we also report the modulation on a shorter time scale of less than 2 minute.

(2) Whistler-mode wave amplitude observed by RBSP-B was well correlated with the observed enhancement in X-ray spectrum in both time and space, with a correlation coefficient of ~0.7 in the plume region.

(3) The observed whistler-mode waves can cause electron precipitation up to MeV and are most effective for precipitating electrons below 100 keV, with bounce-averaged scattering rates up to 10^{-3} s^{-1} at the loss cone. This is consistent with the BARREL observation that only 25–95 keV X-rays, mainly generated by < 100 keV electron precipitation (Jaynes & Usanova, 2019) , are enhanced during this time period. The modulation of the calculated $<D_{\alpha\alpha}>|_{LC}$, which controls the pitch angle distribution and ultimate precipitation rate under the equilibrium state, was remarkably consistent with the modulation of enhancement of BARREL X-rays produced by the energetic electron precipitation.

(4) Modulation of the modeled precipitation due to whistler-mode waves was qualitatively consistent with the enhancement in BARREL X-rays, indicating that whistler-mode waves are responsible for the observed modulation of electron precipitation both in the plumes and the plasma trough.

It was suggested that the density and magnetic field fluctuating on the ULF time-scale might affect the electron precipitation through modulating whistler-mode wave growth (Breneman et al., 2015, 2020; Halford et al., 2015). In our event study, the whistler-mode waves are modulated on longer breathing mode periods than the ULF wave periods (8–30 mHz). The correlation between ULF waves and whistler-mode wave is quite low, indicating that ULF waves play little role in precipitating the electrons into the loss cone in this event. An extensive analysis on a sufficient number of events is needed to determine the accurate role of ULF waves in energetic electron precipitation; however, this is beyond the scope of the current work and left for a future study. Nevertheless, our result has provided strong evidence of whistler-mode wave driven energetic electron precipitation in both plumes and plasma trough regions, which is essential to understand the radiation belt electron loss.

Acknowledgments

This research is supported by the NASA Living With a Star Jack Eddy Postdoctoral Fellowship Program, administered by UCAR's Cooperative Programs for the Advancement of Earth System Science (CPAESS) under award #NNX16AK22G. WL, QM, XS, and LC would like to acknowledge NASA grants of 80NSSC20K0698, 80NSSC19K0845, 80NSSC20K0196, NSF grants of AGS-1847818 and AGS-1723588, and the Alfred P. Sloan Research Fellowship FG-2018-10936. The wave data are obtained from the EMFISIS instrument http://emfisis.physics.uiowa.edu/Flight/. The HOPE and MagEIS data are available from https://www.rbsp-ect.lanl.gov/science/DataDirectories.php. We acknowledge the BARREL team developers of IDL BDAS program for use of BARREL data. BARREL ephemeris, MSPC and FSPC data are available from https://spdf.gsfc.nasa.gov/pub/data/barrel/l2/. The data for the figures are available at: https://figshare.com/articles/dataset/Multi-point_observation_of_energetic_electron_precipitation/17032094

References

Blake, J. B., et al. (2013), The Magnetic Electron Ion Spectrometer (MagEIS) instruments aboard the Radiation Belt Storm Probes (RBSP) spacecraft, Space Sci. Rev., 179, 383–421, doi:10.1007/s11214-013-9991-8.

Borovsky, J. E., & Denton, M. H. (2008). A statistical look at plasmaspheric drainage plumes. Journal of Geophysical Research: Space Physics (1978–2012), 113(A9), n/a-n/a. https://doi.org/10.1029/2007ja012994

Boyd, A. J., Reeves, G. D., Spence, H. E., Funsten, H. O., Larsen, B. A., Skoug, R. M., et al. (2019). RBSP-ECT combined spin-averaged electron flux data product. Journal of Geophysical Research: Space Physics, 124, 9124– 9136. https://doi-org/10.1029/2019JA026733

Breneman, A. W., Halford, A., Millan, R., McCarthy, M., Fennell, J., Sample, J., et al. (2015). Global-scale coherence modulation of radiation-belt electron loss from plasmaspheric hiss. Nature, 523(7559), 193–195. https://doi.org/10.1038/nature14515

Breneman, A. W., Halford, A. J., Millan, R. M., Woodger, L. A., Zhang, X. -J., Sandhu, J. K., et al. (2020). Driving of Outer Belt Electron Loss by Solar Wind Dynamic Pressure Structures: Analysis of Balloon and Satellite Data. Journal of Geophysical Research: Space Physics, 125(12). https://doi.org/10.1029/2020ja028097

Capannolo, L., Li, W., Ma, Q., Chen, L., Shen, X. -C., Spence, H. E., et al. (2019). Direct Observation of Subrelativistic Electron Precipitation Potentially Driven by EMIC Waves. Geophysical Research Letters, 46(22), 12711–12721. https://doi.org/10.1029/2019gl084202

Capannolo, L., Li, W., Ma, Q., Shen, X. -C., Zhang, X. -J., Redmon, R. J., et al. (2019). Energetic Electron Precipitation: Multievent Analysis of Its Spatial Extent During EMIC Wave Activity. Journal of Geophysical Research: Space Physics, 124(4), 2466–2483. https://doi.org/10.1029/2018ja026291

Carpenter, D. L., Anderson, R. R., Calvert, W., & Moldwin, M. B. (2000). CRRES observations of density cavities inside the plasmasphere. Journal of Geophysical Research: Space Physics, 105(A10), 23323–23338. https://doi.org/10.1029/2000ja000013

Chan, K., & Holzer, R. E. (1976). ELF hiss associated with plasma density enhancements in the outer magnetosphere. Journal of Geophysical Research, 81(13), 2267–2274. https://doi.org/10.1029/ja081i013p02267

Chen, A. J., & Wolf, R. A. (1972). Effects on the plasmasphere of a time-varying convection electric field. Planetary and Space Science, 20(4), 483–509. https://doi.org/10.1016/0032-0633(72)90080-3

Chen, L., Li, W., Bortnik, J., & Thorne, R. M. (2012). Amplification of whistler-mode hiss inside the plasmasphere. Geophysical Research Letters, 39(8), n/a-n/a. https://doi.org/10.1029/2012gl051488

Chen, L., Thorne, R. M., Bortnik, J., & Zhang, X. (2016). Nonresonant interactions of electromagnetic ion cyclotron waves with relativistic electrons. Journal of Geophysical Research: Space Physics, 121(10), 9913–9925. https://doi.org/10.1002/2016ja022813

Clilverd, M. A., Duthie, R., Hardman, R., Hendry, A. T., Rodger, C. J., Raita, T., et al. (2015). Electron precipitation from EMIC waves: A case study from 31 May 2013. Journal of Geophysical Research: Space Physics, 120(5), 3618–3631. https://doi.org/10.1002/2015ja021090

Goldstein, J., Sandel, B. R., Thomsen, M. F., Spasojević, M., & Reiff, P. H. (2004). Simultaneous remote sensing and in situ observations of plasmaspheric drainage plumes.

Journal of Geophysical Research: Space Physics (1978–2012), 109(A3). https://doi.org/10.1029/2003ja010281

Halford, A. J., McGregor, S. L., Murphy, K. R., Millan, R. M., Hudson, M. K., Woodger, L. A., et al. (2015). BARREL observations of an ICME-shock impact with the magnetosphere and the resultant radiation belt electron loss. Journal of Geophysical Research: Space Physics, 120(4), 2557–2570. https://doi.org/10.1002/2014ja020873

Hendry, A. T., Rodger, C. J., & Clilverd, M. A. (2017). Evidence of sub-MeV EMIC-driven electron precipitation. Geophysical Research Letters, 44(3), 1210–1218. https://doi.org/10.1002/2016gl071807

Kennel, C. F., & Petschek, H. E. (1966). Limit on stably trapped particle fluxes. Journal of Geophysical Research, 71(1), 1–28. https://doi.org/10.1029/jz071i001p00001

Kepko, L., Spence, H. E., and Singer, H. J., ULF waves in the solar wind as direct drivers of magnetospheric pulsations, Geophys. Res. Lett., 29(8), doi:10.1029/2001GL014405, 2002.

Kepko, L., and H. E. Spence (2003), Observations of discrete, global magnetospheric oscillations directly driven by solar wind density variations, J. Geophys. Res., 108(A6), 1257, doi:10.1029/2002JA009676.

Kepko, L., & Viall, N. M. (2019). The source, significance, and magnetospheric impact of periodic density structures within stream interaction regions. J. Geophys. Res.: Space Physics, 124, 7722–7743. https://doi.org/10.1029/ 2019JA026962.

Kletzing, C. A., Kurth, W. S., Acuna, M., MacDowall, R. J., Torbert, R. B., Averkamp, T., et al. (2013). The Electric and Magnetic Field Instrument Suite and Integrated Science (EMFISIS) on RBSP. Space Science Reviews, 179(1-4), 127–181. https://doi.org/10.1007/s11214-013-9993-6

Kurth, W. S., De Pascuale, S., Faden, J. B., Kletzing, C. A., Hospodarsky, G. B., Thaller, S., & Wygant, J. R. (2015). Electron densities inferred from plasma wave spectra obtained by the Waves instrument on Van Allen Probes. Journal of Geophysical Research: Space Physics, 120, 904–914. https://doi.org/10.1002/2014JA020857

Li, W., Ni, B., Thorne, R. M., Bortnik, J., Green, J. C., Kletzing, C. A., et al. (2013). Constructing the global distribution of chorus wave intensity using measurements of electrons by the POES satellites and waves by the Van Allen Probes. Geophysical Research Letters, 40(17), 4526–4532. https://doi.org/10.1002/grl.50920

Li, W., Shen, X. -C., Ma, Q., Capannolo, L., Shi, R., Redmon, R. J., et al. (2019). Quantification of Energetic Electron Precipitation Driven by Plume Whistler Mode Waves, Plasmaspheric Hiss, and Exohiss. Geophysical Research Letters, 46(7), 3615–3624. https://doi.org/10.1029/2019gl082095

396 Li, Z., Millan, R. M., Hudson, M. K., Woodger, L. A., Smith, D. M., Chen, Y., et al. (2014).
397 Investigation of EMIC wave scattering as the cause for the BARREL 17 January 2013
398 relativistic electron precipitation event: A quantitative comparison of simulation with
399 observations. Geophysical Research Letters, 41(24), 8722–8729.
400 https://doi.org/10.1002/2014gl062273

401 Liang, J., Ni, B., Spanswick, E., Kubyshkina, M., Donovan, E. F., Uritsky, V. M., Thorne, R.
402 M., and Angelopoulos, V. (2011), Fast earthward flows, electron cyclotron harmonic waves,
403 and diffuse auroras: Conjunctive observations and a synthesized scenario, J. Geophys.
404 Res., 116, A12220, doi:10.1029/2011JA017094.

405 Lyons, L. R., Thorne, R. M., and Kennel, C. F. (1972), Pitch-angle diffusion of radiation belt
406 electrons within the plasmasphere, J. Geophys. Res., 77(19), 3455– 3474,
407 doi:10.1029/JA077i019p03455.

408 Lyons, L. R., and Thorne, R. M. (1973), Equilibrium structure of radiation belt electrons, J.
409 Geophys. Res., 78(13), 2142– 2149, doi:10.1029/JA078i013p02142.

410 Ma, Q., Li, W., Thorne, R. M., Bortnik, J., Kletzing, C. A., Kurth, W. S., & Hospodarsky, G.
411 B. (2016). Electron scattering by magnetosonic waves in the inner magnetosphere. Journal of
412 Geophysical Research: Space Physics, 121(1), 274–285. https://doi.org/10.1002/2015ja021992

413 Ma, Q., Connor, H. K., Zhang, X.-J., Li, W., Shen, X.-C., Gillespie, D., et al. (2020), Global
414 survey of plasma sheet electron precipitation due to whistler mode chorus waves in Earth's
415 magnetosphere, Geophysical Research Letters, 47, e2020GL088798,
416 doi:10.1029/2020GL088798

417 Mauk, B. H., Fox, N. J., Kanekal, S. G., Kessel, R. L., Sibeck, D. G., & Ukhorskiy, a A. (2013).
418 Science objectives and rationale for the Radiation Belt Storm Probes mission. Space Science
419 Reviews, 179(1-4), 3–27. https://doi.org/10.1007/s11214-012-9908-y

420 Meredith, N. P., Horne, R. B., Thorne, R. M., Summers, D., and Anderson, R.
421 R. (2004), Substorm dependence of plasmaspheric hiss, J. Geophys. Res., 109, A06209,
422 doi:10.1029/2004JA010387.

423 Moldwin, M. B., Howard, J., Sanny, J., Bocchicchio, J. D., Rassoul, H. K., & Anderson, R. R.
424 (2004). Plasmaspheric plumes: CRRES observations of enhanced density beyond the
425 plasmapause. Journal of Geophysical Research: Space Physics (1978–2012), 109(A5).
426 https://doi.org/10.1029/2003ja010320

427 Millan, R. M., et al. (2013), The Balloon Array for RBSP Relativistic Electron Losses
428 (BARREL), Space Sci. Rev., 179(1-4), 503–530, doi:10.1007/s11214-013-9971-z.

429 Jaynes, A., & Usanova, M. E. (2019). The Dynamic Loss of Earth's Radiation Belts.

Ni, B., R. M. Thorne, Y. Y. Shprits, and J. Bortnik (2008), Resonant scattering of plasma sheet electrons by whistler-mode chorus: Contribution to diffuse auroral precipitation, Geophys. Res. Lett., 35, L11106, doi:10.1029/2008GL034032.

Ni, B., R. M. Thorne, N. P. Meredith, R. B. Horne, and Y. Y. Shprits (2011), Resonant scattering of plasma sheet electrons leading to diffuse auroral precipitation: 2. Evaluation for whistler mode chorus waves, J. Geophys. Res., 116, A04219, doi:10.1029/2010JA016233.

Ni, B., Bortnik, J., Thorne, R. M., Ma, Q., & Chen, L. (2013). Resonant scattering and resultant pitch angle evolution of relativistic electrons by plasmaspheric hiss. Journal of Geophysical Research: Space Physics, 118, 7740–7751. https://doi.org/10.1002/2013JA019260

Nishimura, Y., et al. (2010), Identifying the driver of pulsating aurora, Science, 330, 81–84.

Qin, M., Hudson, M., Millan, R., Woodger, L., & Shekhar, S. (2018). Statistical Investigation of the Efficiency of EMIC Waves in Precipitating Relativistic Electrons. Journal of Geophysical Research: Space Physics, 123(8), 6223–6230. https://doi.org/10.1029/2018ja025419

Qin, M., Hudson, M., Li, Z., Millan, R., Shen, X., Shprits, Y., et al. (2019). Investigating Loss of Relativistic Electrons Associated With EMIC Waves at Low L Values on 22 June 2015. Journal of Geophysical Research: Space Physics, 124(6), 4022–4036. https://doi.org/10.1029/2018ja025726

Qin, M., Hudson, M., Millan, R., Woodger, L., & Shen, X. (2020). Statistical Dependence of EMIC Wave Scattering on Wave and Plasma Parameters. Journal of Geophysical Research: Space Physics, 125(4). https://doi.org/10.1029/2020ja027772

Shi, R., Li, W., Ma, Q., Green, A., Kletzing, C. A., Kurth, W. S., et al. (2019). Properties of whistler mode waves in Earth's plasmasphere and plumes. Journal of Geophysical Research: Space Physics, 124, 1035– 1051. https://doi.org/10.1029/2018JA026041

Spence, H., et al. (2013), Science goals and overview of the Radiation Belt Storm Probes (RBSP) Energetic Particle, Composition, and Thermal Plasma (ECT) suite on NASA's Van Allen Probes mission, Space Sci. Rev., 179(1-4), 311–336, doi:10.1007/s11214-013-0007-5.

Su, Z., Liu, N., Zheng, H., Wang, Y., & Wang, S. (2018). Large-Amplitude Extremely Low Frequency Hiss Waves in Plasmaspheric Plumes. Geophysical Research Letters, 45(2), 565–577. https://doi.org/10.1002/2017gl076754

Summers, D., and R. M. Thorne (2003), Relativistic electron pitch-angle scattering by electromagnetic ion cyclotron waves during geomagnetic storms, J. Geophys. Res., 108(A4), 1143, doi:10.1029/2002JA009489.

Summers, D., Ni, B., Meredith, N. P., Horne, R. B., Thorne, R. M., Moldwin, M. B., and Anderson, R. R. (2008), Electron scattering by whistler- mode ELF hiss in plasmaspheric plumes, J. Geophys. Res., 113, A04219, doi:10.1029/2007JA012678.

Thorne, R. M., E. J. Smith, R. K. Burton, and R. E. Holzer (1973), Plasmaspheric hiss, J. Geophys. Res., 78, 1581

Thorne, M., R., Church, S. R., & Gorney, and D. J. (1979). On the origin of plasmaspheric hiss: The importance of wave propagation and the plasmapause. J. Geophys. Res., A9(84). https://doi.org/10.1029/ja084ia09p05241

Tsyganenko (1989). A magnetospheric magnetic field model with a warped tail current sheet, Planetary and Space Science, Volume 37, Issue 1, Pages 5-20, ISSN 0032-0633, https://doi.org/10.1016/0032-0633(89)90066-4.

Woodger, L. A., A. J. Halford, R. M. Millan, M. P. McCarthy, D. M. Smith, G. S. Bowers, J. G. Sample, B. R. Anderson, and X. Liang (2015), A summary of the BARREL campaigns: Technique for studying electron precipitation, J. Geophys. Res. Space Physics, 120, 4922–4935, doi:10.1002/2014JA020874.

Zhang, W., Fu, S., Gu, X., Ni, B., Xiang, Z., Summers, D., et al. (2018). Electron Scattering by Plasmaspheric Hiss in a Nightside Plume. Geophysical Research Letters, 45(10), 4618–4627. https://doi.org/10.1029/2018gl077212

Zhang, W., Ni, B., Huang, H., Summers, D., Fu, S., Xiang, Z., et al. (2019). Statistical Properties of Hiss in Plasmaspheric Plumes and Associated Scattering Losses of Radiation Belt Electrons. Geophysical Research Letters, 46(11), 5670–5680. https://doi.org/10.1029/2018gl081863

Figures and Captions

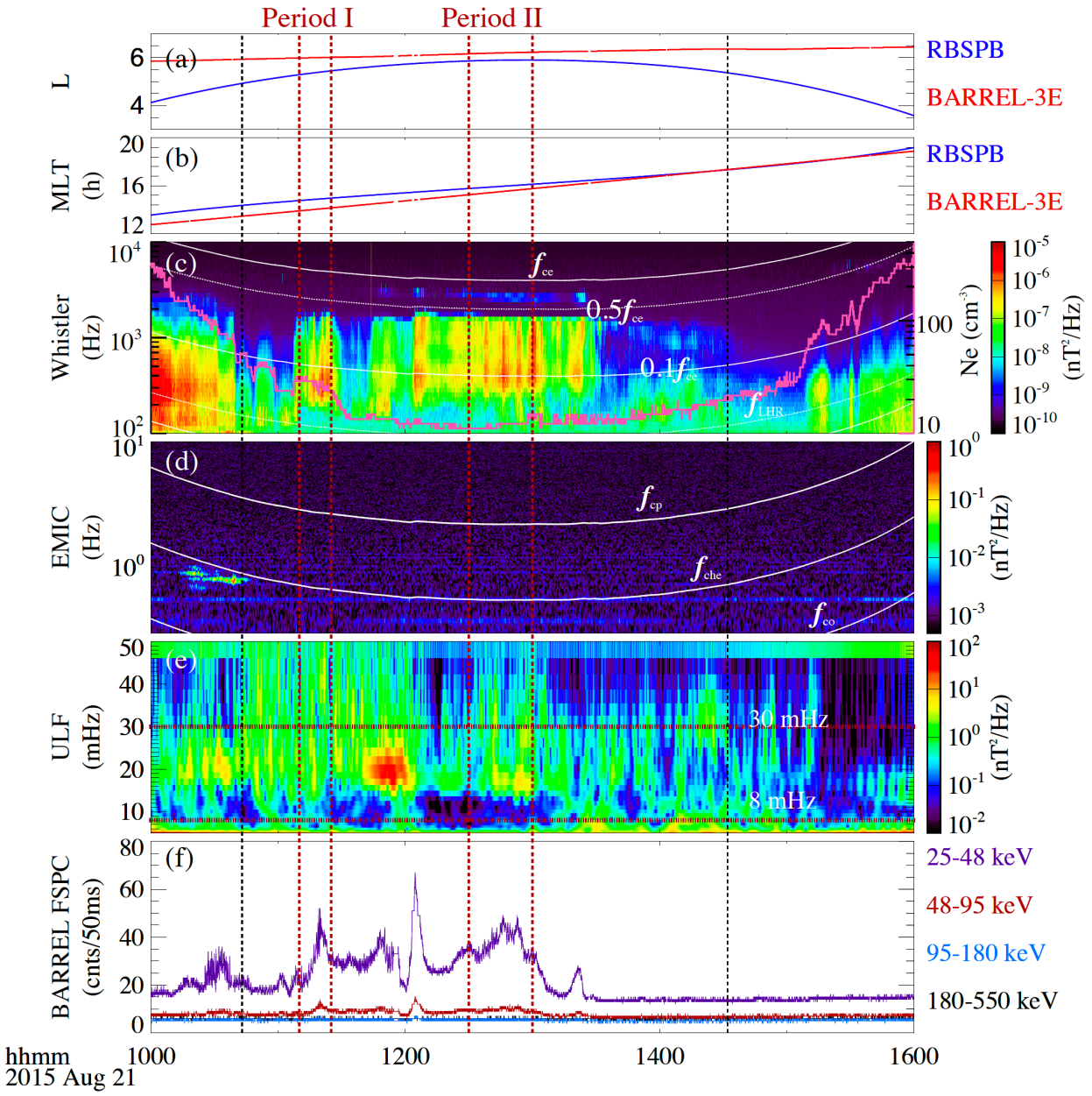

Figure 1. (a) *L* shells of RBSP-B (blue) and BARREL-3E (red) based on the T89 magnetic field model. (b) MLT of RBSP-B (blue) and BARREL-3E (red). (c) Magnetic spectral density observed by the Waveform Receiver (WFR) onboard RBSP-B. In panel (c), the white lines represent the electron cyclotron frequency (f_{ce}), 0.5 f_{ce}, 0.1 f_{ce} and f_{LHR} from top to bottom. The superimposed magenta line represents the electron number density inferred from the upper hybrid resonance frequency (Kurth et al., 2015) measured by the High-Frequency Receiver (HFR). (d–e) Magnetic spectral density calculated from the fluxgate magnetometer onboard RBSP-B. The white lines in panel (d) indicate proton, helium, and oxygen cyclotron frequencies. The horizontal lines in panel

497 (e) indicate 8 mHz and 30 mHz. ULF waves within this frequency range were selected to show
498 modulations below 2 min. (f) BARREL fast spectrum X-rays at energies of 25–48 (purple), 48–95
499 (red), 95–180 (blue), and 180–550 keV (black). The black vertical dashed lines represent the
500 conjunction region when the separation between RBSP-B and BARREL was within $\Delta L = 1$ and
501 $\Delta\mathrm{MLT} = 1$ over 10:40–14:32 UT. The red vertical dashed lines represent the times when RBSP
502 was in the plume region (Period I) and plasma trough (Period II), which are analyzed in detail in
503 Figures 5 and 6.
504

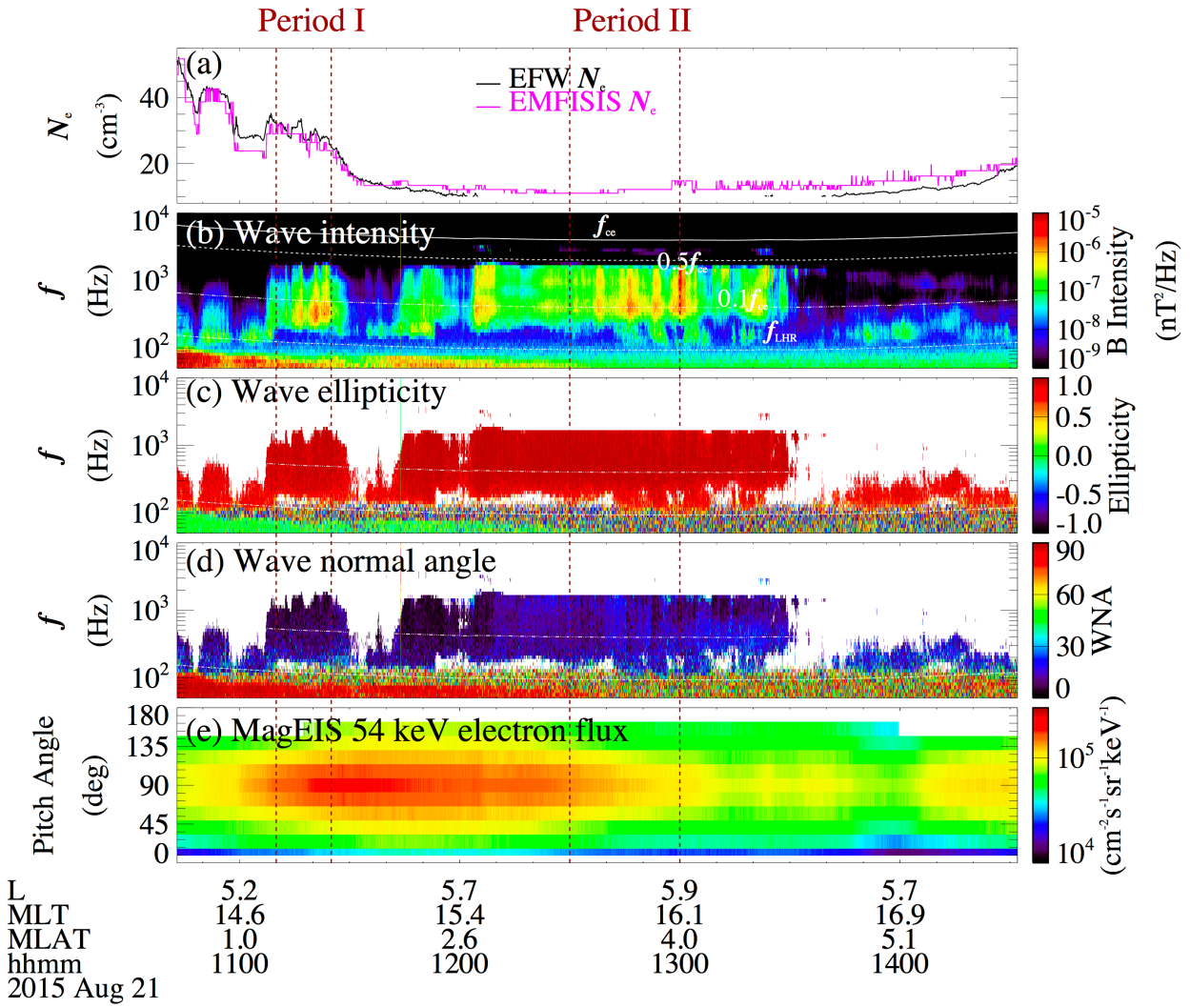

Figure 2. (a) Total electron density observed near the equator by RBSP-B, where the magenta solid line represents density inferred from the upper hybrid resonance frequency, and the black solid line represents density inferred from the spacecraft potential. (b) Frequency-time spectrogram of magnetic spectral density, (c) ellipticity, and (d) wave normal angle (WNA), where the white lines represent the electron cyclotron frequency f_{ce}, 0.5 f_{ce}, 0.1 f_{ce}, and lower hybrid resonance frequency (f_{LHR}) from top to bottom. (e) Pitch angle spectrogram of 54 keV electron flux measured by MagEIS. Period I represents the time when RBSP-B was in the plume region and observed hiss waves, and Period II represents the time when RBSP-B was in the plasma trough and observed chorus waves.

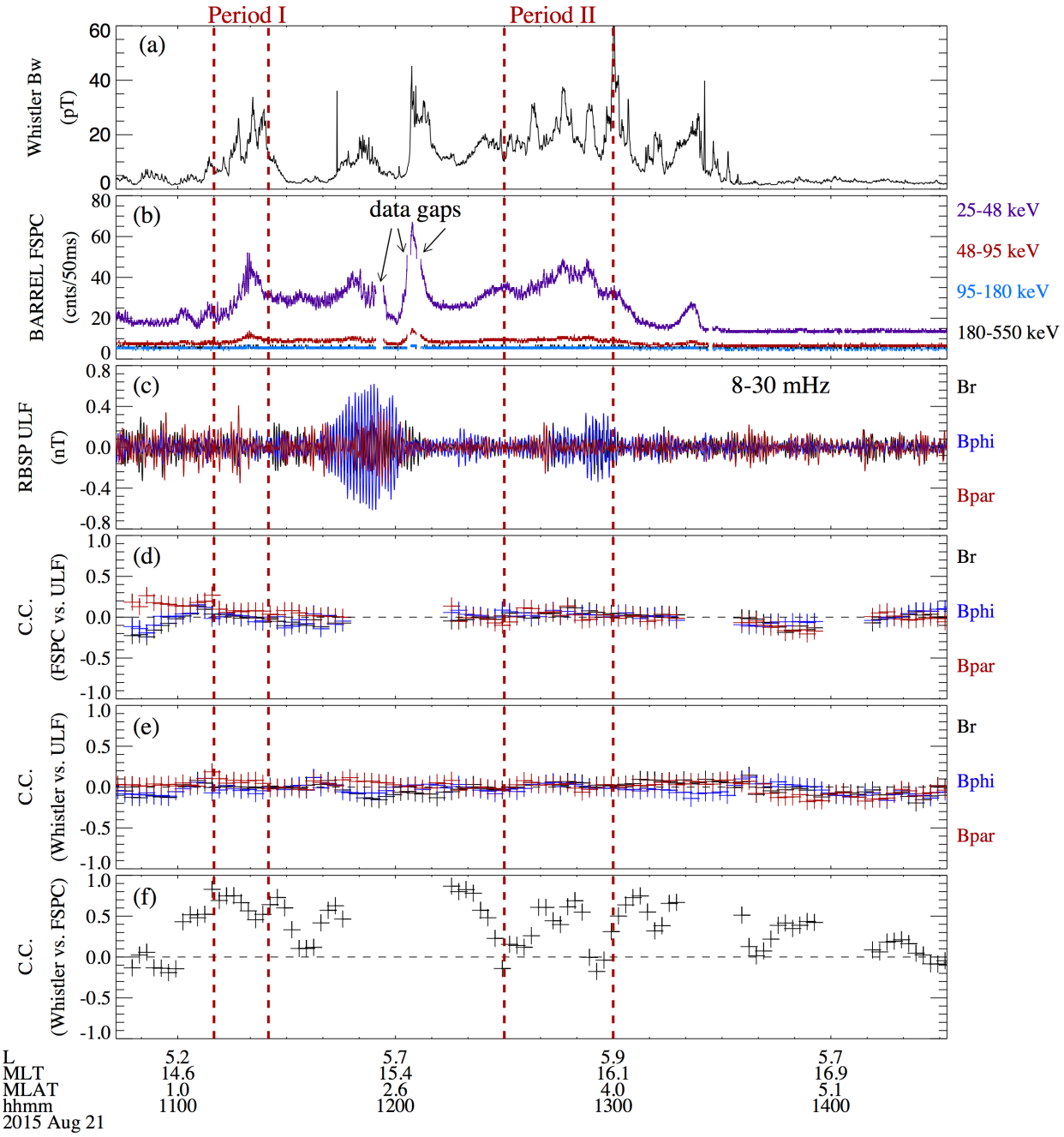

Figure 3. (a) Whistler-mode wave amplitude observed by RBSP-B with time resolution of 6 s. (b) 30 s smoothed BARREL fast spectrum X-rays, with arrows indicating data gaps. (c) Wave amplitude of poloidal (black), toroidal (blue) and compressional (red) 8–30 mHz ULF wave components. (d) Correlation coefficients between X-ray count rate and 8–30 mHz ULF wave amplitudes. (e) Correlation coefficients between whistler-mode wave amplitude and 8–30 mHz ULF wave amplitudes (black, blue and red cross signs represent poloidal, toroidal, and compressional components respectively). (f) Correlation coefficients between whistler-mode wave amplitude and X-ray count rate. The gaps in panel (d) and panel (f) are caused by the data gaps in BARREL fast spectrum X-rays shown in panel (b). Period I and II are the same as in Figure 1.

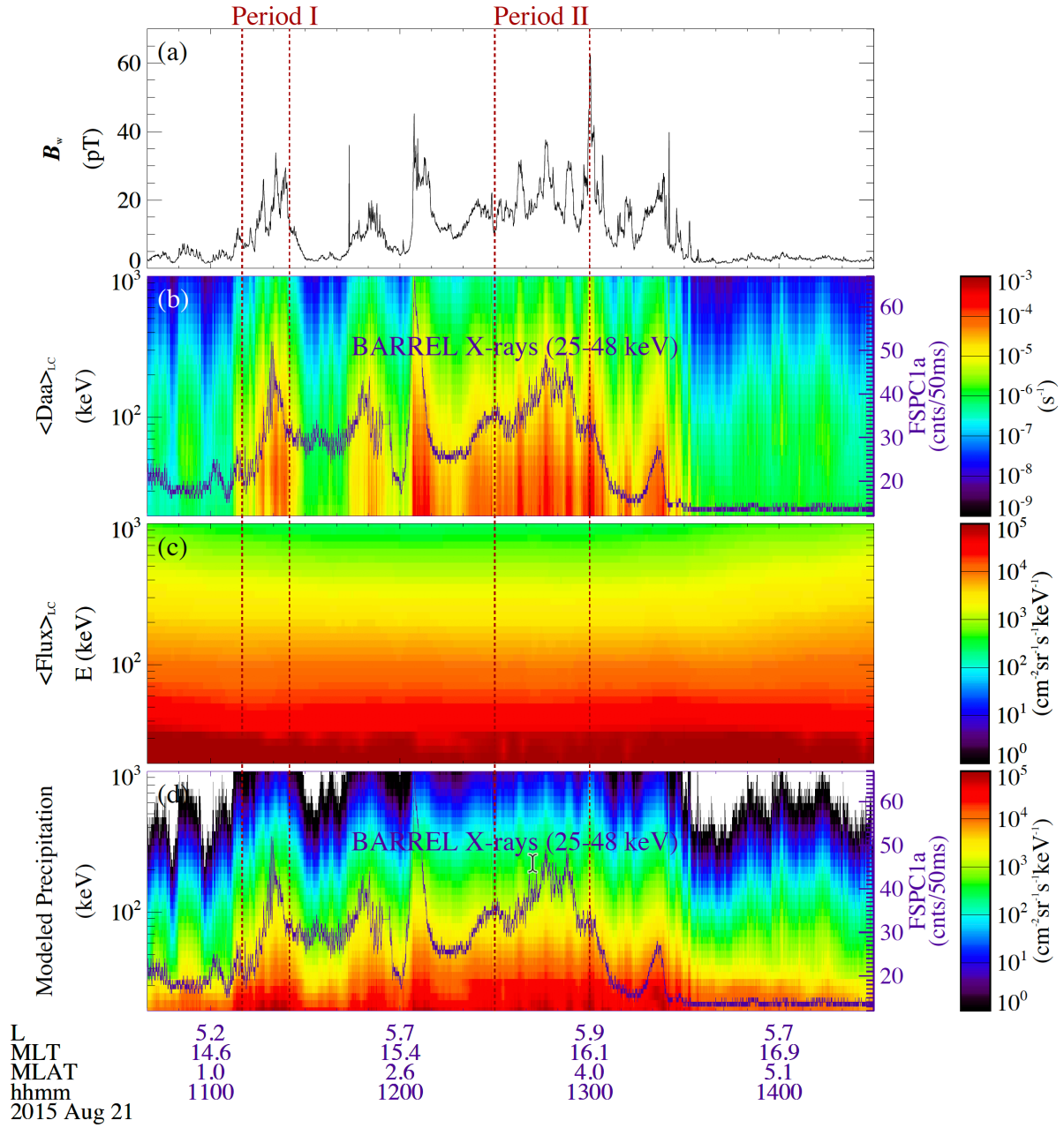

Figure 4. (a) Whistler-mode wave amplitude in the plume region. (b) Energy spectrogram of bounce-averaged pitch angle diffusion coefficients at the loss cone, (c) electron flux at the loss cone using the combined RBSP-ECT data product (Boyd et al., 2019) of HOPE and MagEIS, and (d) modeled electron precipitation under the quasi-equilibrium state. The superimposed purple line in panel (b) and (d) is the observed count rate of 25–48 keV BARREL X-rays. Periods I and II are the same as those marked in the Figure 1.

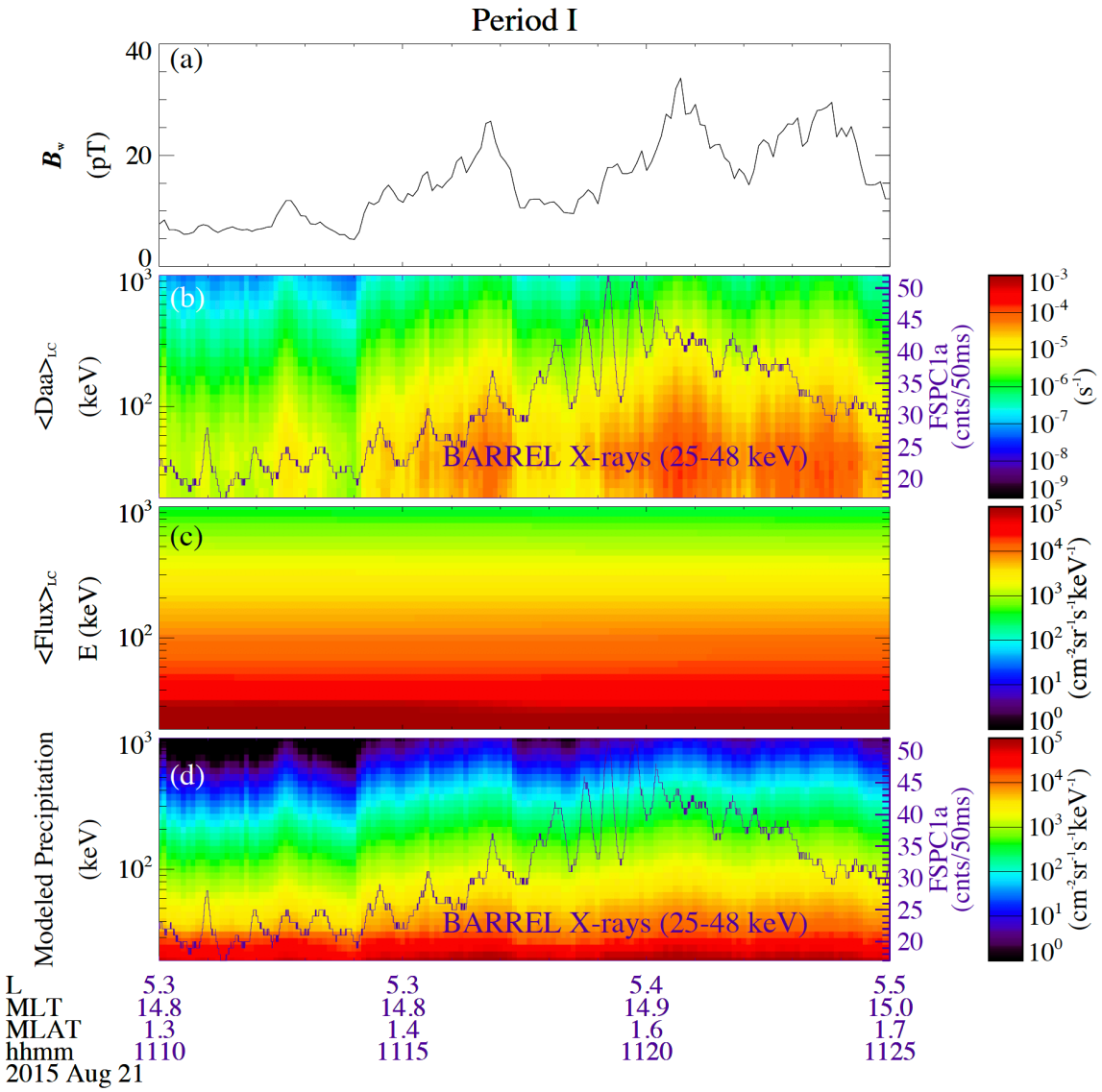

Figure 5. Same as Figure 4, except in the plume region during Period I.

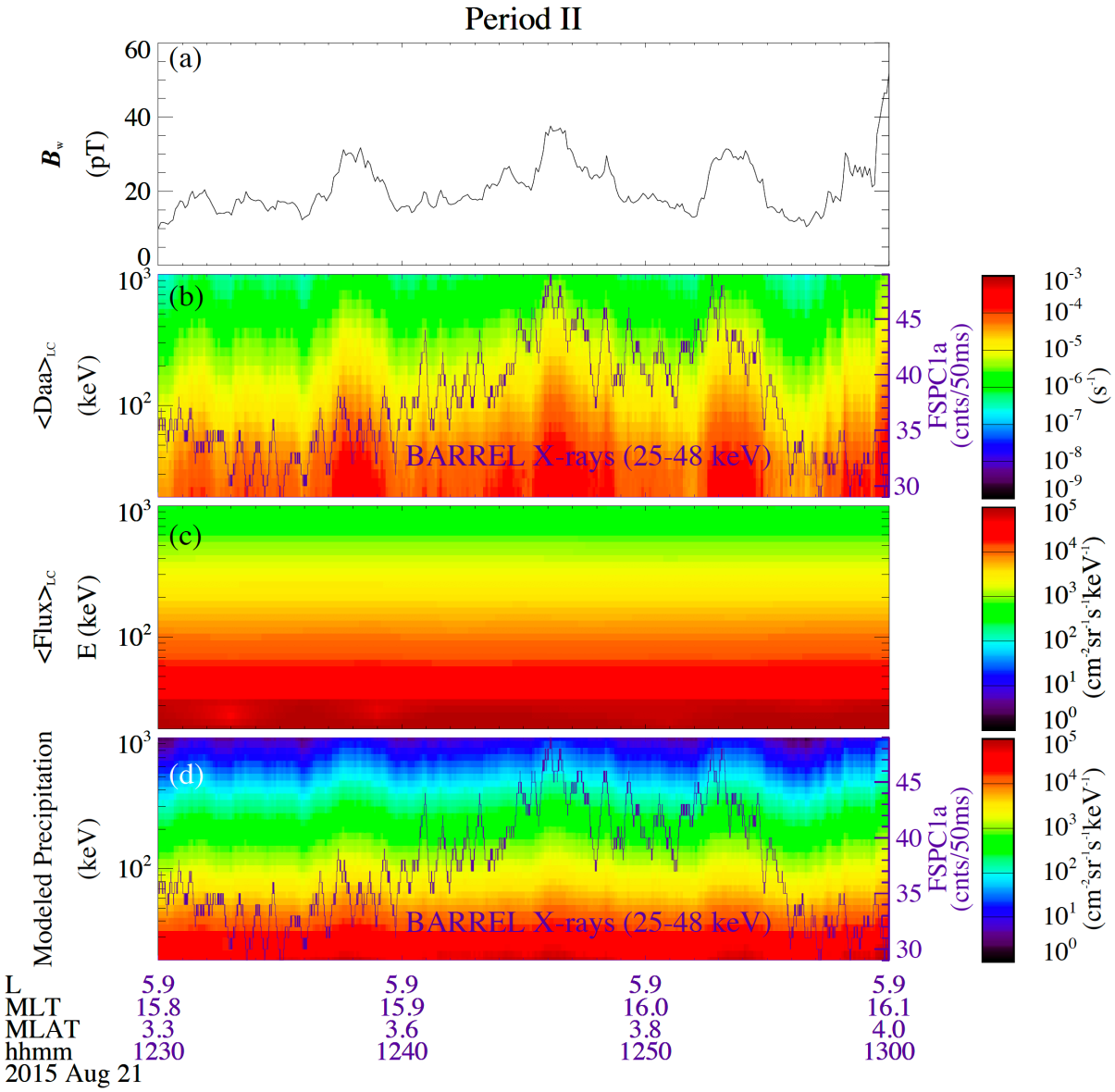

Figure 6. Same as Figure 4, except in the plasma trough during Period II.

Figure 1.

Period I
Period II
(a)
L
6
4
RBSPB
BARREL-3E
(b)
MLT (h)
20
16
12
RBSPB
BARREL-3E
(c)
Whistler (Hz)
10^4
10^3
10^2
f_{ce}
$0.5f_{ce}$
$0.1f_{ce}$
f_{LHR}
100
10
Ne (cm^{-3})
10^{-5}
10^{-6}
10^{-7}
10^{-8}
10^{-9}
10^{-10}
(nT^2/Hz)
(d)
EMIC (Hz)
10^1
10^0
f_{cp}
f_{che}
f_{co}
10^0
10^{-1}
10^{-2}
10^{-3}
(nT^2/Hz)
(e)
ULF (mHz)
50
40
30
20
10
30 mHz
8 mHz
10^2
10^1
10^0
10^{-1}
10^{-2}
(nT^2/Hz)
(f)
BARREL FSPC (cnts/50ms)
80
60
40
20
0
25-48 keV
48-95 keV
95-180 keV
180-550 keV
hhmm
1000
1200
1400
1600
2015 Aug 21

Figure 2.

Period I
Period II
(a)
EFW N_e
EMFISIS N_e
N_e (cm^{-3})
40
20
(b) Wave intensity
f_{ce}
$0.5f_{ce}$
$0.1f_{ce}$
f_{LHR}
f (Hz)
10^4
10^3
10^2
B Intensity (nT^2/Hz)
10^{-5}
10^{-6}
10^{-7}
10^{-8}
10^{-9}
(c) Wave ellipticity
Ellipticity
1.0
0.5
0.0
-0.5
-1.0
(d) Wave normal angle
WNA
90
60
30
0
(e) MagEIS 54 keV electron flux
Pitch Angle (deg)
180
135
90
45
0
($cm^{-2}s^{-1}sr^{-1}keV^{-1}$)
10^5
10^4
L 5.2 5.7 5.9 5.7
MLT 14.6 15.4 16.1 16.9
MLAT 1.0 2.6 4.0 5.1
hhmm 1100 1200 1300 1400
2015 Aug 21

Figure 3.

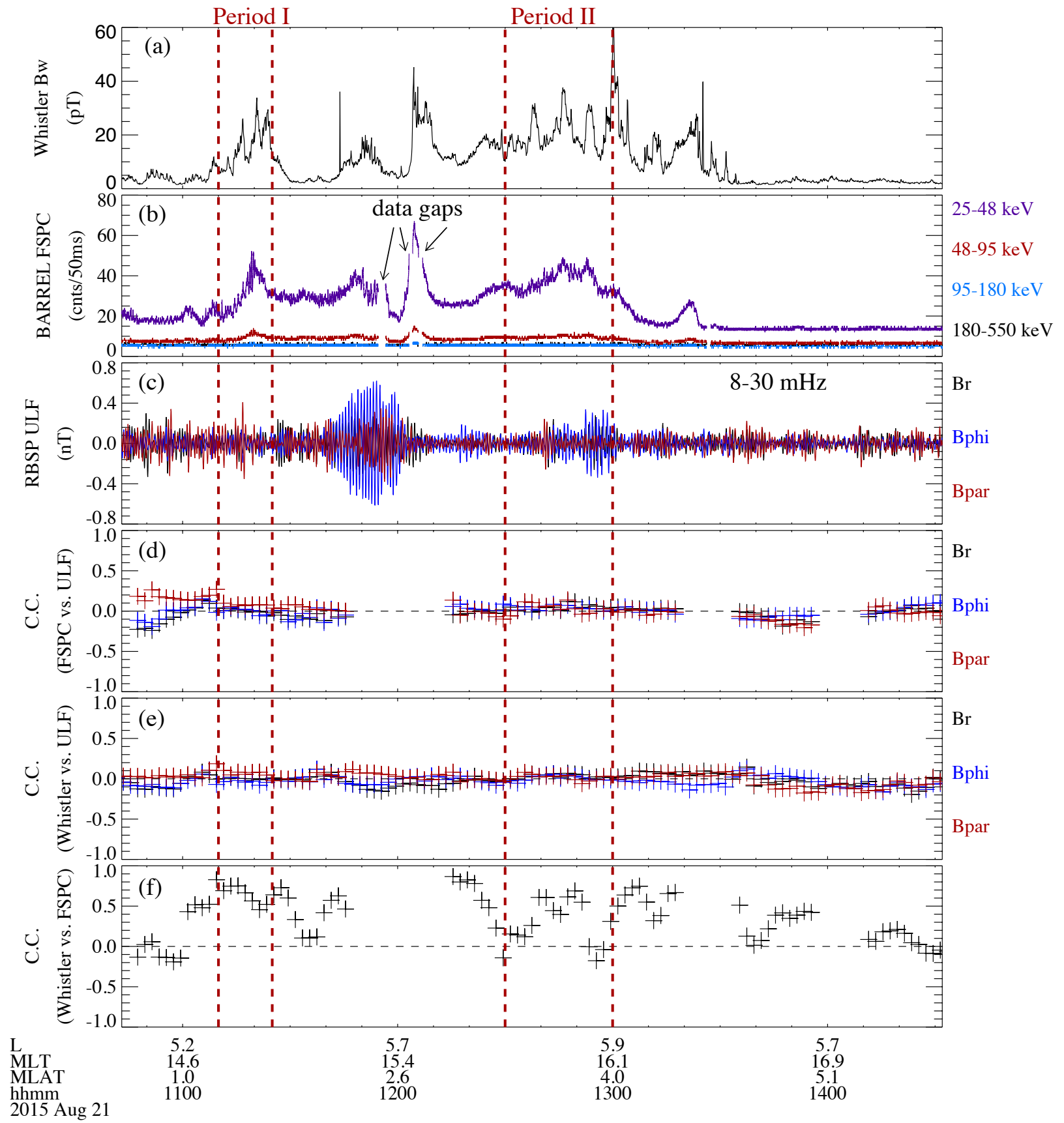
Period I
Period II
(a)
Whistler Bw
(pT)
60
40
20
0
(b)
data gaps
BARREL FSPC
(cnts/50ms)
80
60
40
20
0
25-48 keV
48-95 keV
95-180 keV
180-550 keV
(c)
8-30 mHz
RBSP ULF
(nT)
0.8
0.4
0.0
-0.4
-0.8
Br
Bphi
Bpar
(d)
C.C.
(FSPC vs. ULF)
1.0
0.5
0.0
-0.5
-1.0
Br
Bphi
Bpar
(e)
C.C.
(Whistler vs. ULF)
1.0
0.5
0.0
-0.5
-1.0
Br
Bphi
Bpar
(f)
C.C.
(Whistler vs. FSPC)
1.0
0.5
0.0
-0.5
-1.0
L
MLT
MLAT
hhmm
5.2
14.6
1.0
1100
5.7
15.4
2.6
1200
5.9
16.1
4.0
1300
5.7
16.9
5.1
1400
2015 Aug 21

Figure 4.

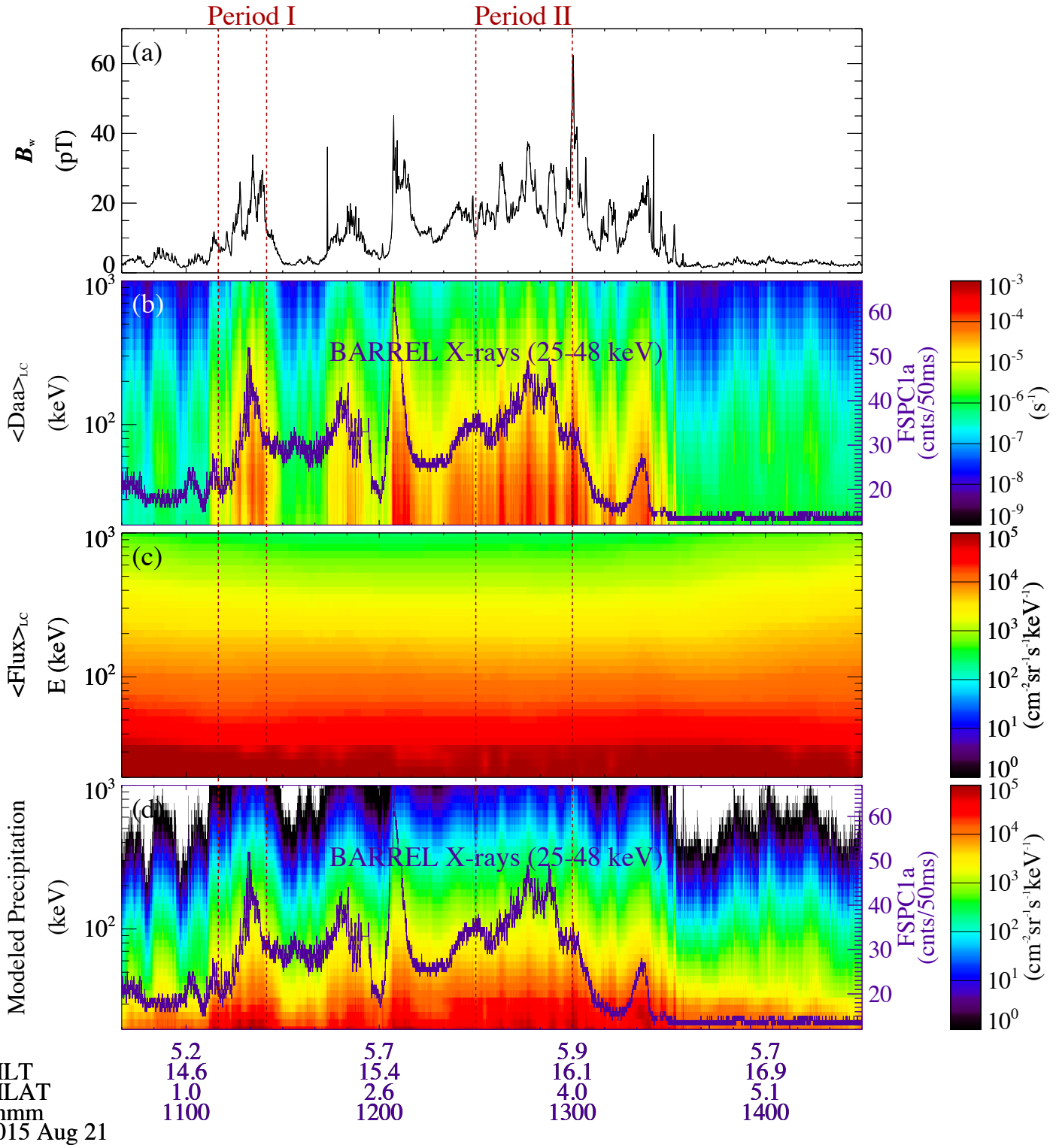
Period I
Period II
(a)
B_w (pT)
60
40
20
0
(b)
BARREL X-rays (25-48 keV)
<Daa>$_{LC}$ (keV)
10^3
10^2
FSPC1a (cnts/50ms)
60
50
40
30
20
10^{-3}
10^{-4}
10^{-5}
10^{-6}
10^{-7}
10^{-8}
10^{-9}
(s^{-1})
(c)
<Flux>$_{LC}$ E (keV)
10^3
10^2
10^5
10^4
10^3
10^2
10^1
10^0
($cm^{-2}sr^{-1}s^{-1}keV^{-1}$)
(d)
BARREL X-rays (25-48 keV)
Modeled Precipitation (keV)
10^3
10^2
FSPC1a (cnts/50ms)
60
50
40
30
20
10^5
10^4
10^3
10^2
10^1
10^0
($cm^{-2}sr^{-1}s^{-1}keV^{-1}$)
L 5.2 5.7 5.9 5.7
MLT 14.6 15.4 16.1 16.9
MLAT 1.0 2.6 4.0 5.1
hhmm 1100 1200 1300 1400
2015 Aug 21

Figure 5.

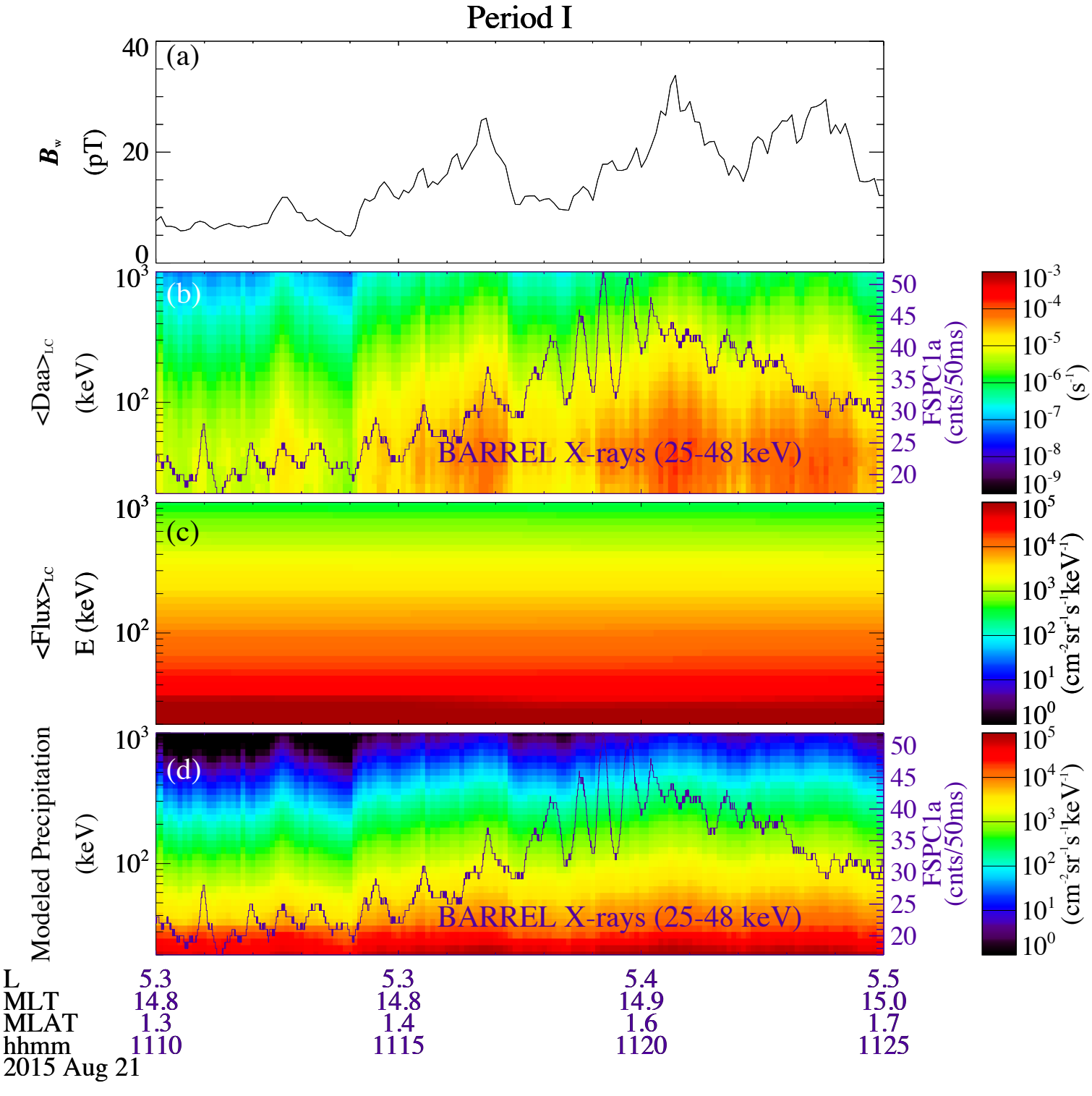
Period I
(a)
B_w (pT)
40
20
0
(b)
<Daa>$_{LC}$ (keV)
10^3
10^2
BARREL X-rays (25-48 keV)
FSPC1a (cnts/50ms)
50
45
40
35
30
25
20
10^{-3}
10^{-4}
10^{-5}
10^{-6}
10^{-7}
10^{-8}
10^{-9}
(s^{-1})
(c)
<Flux>$_{LC}$ E (keV)
10^3
10^2
10^5
10^4
10^3
10^2
10^1
10^0
($cm^{-2}sr^{-1}s^{-1}keV^{-1}$)
(d)
Modeled Precipitation (keV)
10^3
10^2
BARREL X-rays (25-48 keV)
FSPC1a (cnts/50ms)
50
45
40
35
30
25
20
10^5
10^4
10^3
10^2
10^1
10^0
($cm^{-2}sr^{-1}s^{-1}keV^{-1}$)
L 5.3 5.3 5.4 5.5
MLT 14.8 14.8 14.9 15.0
MLAT 1.3 1.4 1.6 1.7
hhmm 1110 1115 1120 1125
2015 Aug 21

Figure 6.

Period II

(a)

B_w (pT)

60
40
20
0

(b)

<Daa>$_{LC}$ (keV)

10^3
10^2

BARREL X-rays (25-48 keV)

45
40
35
30

FSPC1a (cnts/50ms)

10^{-3}
10^{-4}
10^{-5}
10^{-6}
10^{-7}
10^{-8}
10^{-9}
(s^{-1})

(c)

<Flux>$_{LC}$ E (keV)

10^3
10^2

10^5
10^4
10^3
10^2
10^1
10^0
(cm^{-2}sr^{-1}s^{-1}keV^{-1})

(d)

Modeled Precipitation (keV)

10^3
10^2

BARREL X-rays (25-48 keV)

45
40
35
30

FSPC1a (cnts/50ms)

10^5
10^4
10^3
10^2
10^1
10^0
(cm^{-2}sr^{-1}s^{-1}keV^{-1})

L	5.9	5.9	5.9	5.9
MLT	15.8	15.9	16.0	16.1
MLAT	3.3	3.6	3.8	4.0
hhmm	1230	1240	1250	1300

2015 Aug 21